Article:
Schenk, AS, Eiben, S, Goll, M et al. (6 more authors) (2017) Virus-directed formation of electrocatalytically active nanoparticle-based Co_3O_4 tubes. Nanoscale, 9 (19). pp. 6334-6345. ISSN 2040-3364

https://doi.org/10.1039/C7NR00508C

Virus-directed formation of electrocatalytically active nanoparticle-based Co_3O_4 tubes

A. S. Schenk,*[,a] S. Eiben,[b] M. Goll,[a] L. Reith,[a] A. N. Kulak,[c] F. C. Meldrum,[c] H. Jeske,[b] C. Wege,[b] and S. Ludwigs*[,a]

Spinel-type Co_3O_4 finds applications in a wide range of fields, including clean energy conversion, where nanostructured Co3O4 may provide a cost-efficient alternative to platinum- and iridium-based catalysts for electrocatalytic water-splitting. We here describe a novel strategy in which basic cobalt carbonate – a precursor to Co_3O_4 – is precipitated as sheet-like structures and microspheres covered with fine surface protrusions, via ammonium carbonate decomposition at room temperature. Importantly, these mild reaction conditions enable us to employ bio-inspired templating approaches to further control the mineral structure. Rod-like tobacco mosaic viruses (TMV) were used as biotemplates for mineral deposition, where we profit from the ability of Co (II) ions to mediate the ordered assembly of the virus nanorods to create complex tubular superstructures of TMV/ basic cobalt carbonate. Calcination of these tubules is then achieved with retention of the gross morphology, and generates a hierarchically-structured solid comprising interconnected Co_3O_4 nanoparticles. Evaluation of these Co_3O_4 materials as electrocatalysts for the oxygen evolution reaction (OER) demonstrates that the activity of Co_3O_4 prepared by calcination of ammonia diffusion-grown precursors in both, the absence or presence of TMV exceeds that of a commercial nanopowder.

Introduction

Cobalt (II,III) oxide has interesting magnetic and semiconductor properties, leading to potential applications in areas such as battery electrodes,[1] sensor materials[2] and heterogeneous catalysis[3]. One of the most exciting uses of Co_3O_4, however, is in the topical area of sustainable energy conversion systems, where its bifunctional catalytic activity towards both the oxygen evolution and oxygen reduction reaction (OER and ORR) in electrocatalytic water splitting renders it a robust and cost-efficient alternative to expensive materials containing elements such as Pt, Ir and Ru.[4, 5] The catalytic activity of Co_3O_4 strongly depends on structural parameters including its surface area, size and morphology.[3, 6] A range of synthesis methods including electrodeposition,[7] spray pyrolysis,[8] chemical vapor deposition,[9] atomic layer deposition,[10] and transformation of precursors such as Co (II) salts[11-14] and coordination compounds[15] have therefore been explored to generate cobalt oxide nanostructures. With their tendency towards the formation of low-dimensional, anisotropic structures with high surface areas,[16, 17] and the production of non-toxic gaseous products during their thermal conversion into Co_3O_4, the precursor-led methods based on the decomposition of cobalt hydroxides, carbonates and basic carbonates are particularly attractive.

However, (basic) cobalt carbonates with defined morphology are most commonly prepared under solvothermal conditions requiring elevated temperatures and a pressurized reaction container.[16, 18-20]

In this article we introduce a novel synthesis of basic cobalt carbonate ($Co(CO_3)_x(OH)_y$) – based on the decomposition of solid ammonium carbonate – that operates at room temperature and in aqueous solution (Figure 1A). That precipitation occurs slowly and under ambient conditions then affords us the ability to control the process using bio-inspired mineralization strategies, where we use wild-type tobacco mosaic virus (TMV) to direct the structure of the product mineral. It is now well-recognized that organisms use both soluble and insoluble organic additives to facilitate the formation of biominerals, where these characteristically exhibit complex morphologies, composite structures[21, 22] and hierarchical organization spanning multiple length scales.[23] These key control strategies can be successfully translated to synthetic systems, where a wide range of small molecules,[24] polyelectrolytes[25-29] and double hydrophilic block copolymers[30, 31] have been employed as simple mimics of soluble biomacromolecules. Organized insoluble matrices such as Langmuir monolayers and self-assembled monolayers have afforded control over crystal orientation,[32, 33] while nanostructured polymer films[34, 35] and biological templates such as virus particles,[36, 37] bacterial S-layers,[38] pollen grains,[39] sea urchin skeletal elements,[40, 41] and fungi[42] have been used to generate solids with complex morphologies.

With their rod-like morphologies, rigid supramolecular structures, and stability over a wide pH range and temperatures up to 80 °C,[43] TMV nanorods offer many attractive features as templates. Constructed from a single strand of RNA and 2130 identical coat protein (CP) molecules that are arranged in a right-handed helix,[44] each virus particle is of dimensions 300 nm $\times$ 18 nm, and exhibits a central channel of width 4 nm.[44] TMV-like derivatives can also be formed *in vitro* by bottom-up assembly of CP units with RNA,[45] which enables tailored modifications of both their size and shape,[46] and the introduction of selected functional groups.[47] Key to their performance as templates, the surfaces of TMV particles are patterned with chemically-distinct nanoscale domains that can specifically bind different materials and ions,[48-50] and thus mediate the preparation of a range of bio-inorganic hybrid materials based on metals such as Pt,[51] Co,[52] and Ni[53] and metal oxides including ZnO,[54, 55] SiO_2,[56] TiO_2,[57] and RuO_2.[58] While common templating strategies are based on coating individual virus particles or viruses immobilized on substrates with inorganic materials, our studies on TMV-mediated deposition of basic cobalt carbonates take these experiments one stage further, and exploit the ability of Co (II) ions not only to bind to TMV particles but to drive their ordered association in solution. These Co^{2+}/ TMV complexes are then used to generate hierarchically-structured rod-shaped and tubular $Co(CO_3)_x(OH)_y$/ virus composites, whose conversion into spinel-type cobalt oxide by annealing can be achieved with conservation of morphology. Finally, the electrocatalytic activity of the products towards the oxygen evolution reaction (OER) is studied, and is shown to outperform a commercial powder.

Experimental

Full details of the experimental methods are provided in the Supporting Information.

Briefly, basic cobalt carbonate was deposited by exposing $CoCl_2$-solutions to ammonium carbonate vapor at room temperature according to two different protocols:

(i) in the absence of additives

(ii) in the presence of tobacco mosaic viruses as nanoparticular templates with a rigid-rod supramolecular structure.

The mineralization products were then converted into cobalt (II,III) oxide by calcination at 400°C. Dynamic light scattering (DLS) and transmission electron microscopy were used to systematically study the aggregation behavior of tobacco mosaic viruses in $CoCl_2$-solutions with different concentrations. The structure and chemical composition of the mineral precipitates before and after annealing were characterized using a range of imaging, spectroscopic and x-ray diffraction techniques.

In view of potential applications, the calcination products were examined as electrocatalysts for the oxygen evolution reaction (OER). Therefore, the Co_3O_4 particles were immobilized on a glassy carbon rotating disc electrode (GC-RDE) and overpotentials for the OER were determined from electrochemical measurements in a 3-electrode glass cell under alkaline conditions.

Results

1. Preparation of Co_3O_4 via Basic Cobalt Carbonate

Experiments were first conducted to explore the synthesis of basic cobalt carbonate under ambient conditions, and its subsequent conversion to catalytically-active Co_3O_4 by heat treatment. Basic cobalt carbonate was precipitated on exposure of a 100 mM solution of $CoCl_2 \cdot 6H_2O$ to NH_3 and CO_2 vapor released from the slow decomposition of solid ammonium carbonate (Figure 1A). Scanning electron microscopy (SEM) analysis of the precipitates generated after 2 days revealed the formation of mineral particles with two distinct morphologies: extended film-like structures several μm in thickness (which formed at the air/water interface) and agglomerated 200 nm – 2 μm spherical particles (which formed in bulk and were the principal product) (Figs. 1B – 1D). The majority of the film fragments were found to be bent or even curled up (Figs. 1B and 1C), where this may originate from non-uniform shrinking due to the differences in surface roughness and material density between the two faces of the flakes (Fig. S1).[59,60]

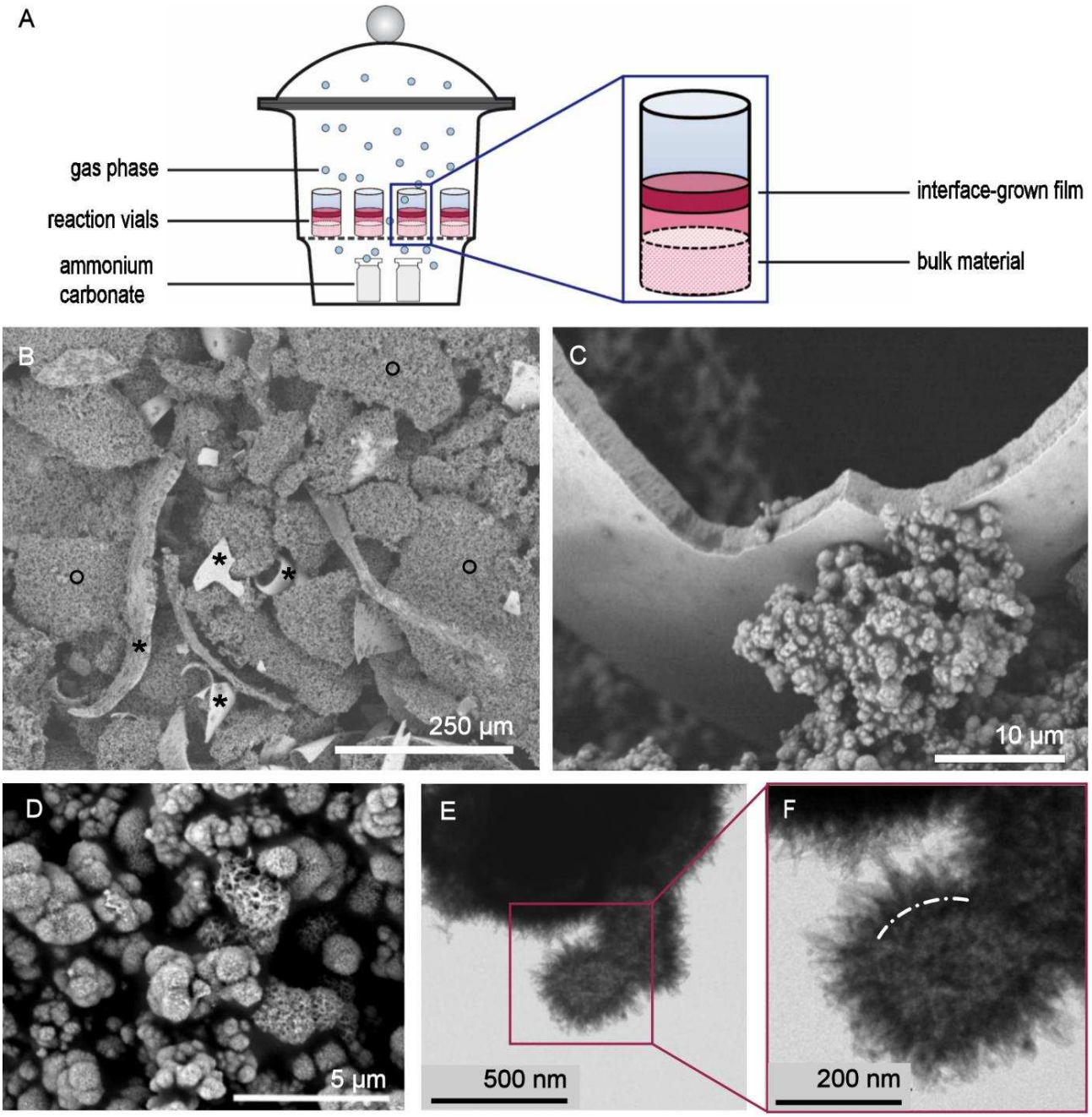

Figure 1. Morphology of basic cobalt carbonate deposited from a 100 mM Co^{2+} solution via ammonium carbonate diffusion. A) Schematic illustration of the experimental setup highlighting the origin of bulk and interface materials within the reaction vial. B) SEM image showing the reaction products, where the sample comprises both sheet-like (*) and spherical aggregates (o). C) Higher magnification micrograph showing the cross section of a sheet. D) SEM images and E) and F) TEM images of the spherical aggregates, where the TEM images show the fibre-like protrusions on the surfaces of the particles. The white dashed line marks the edge of a microsphere, from which the fibres appear to originate.

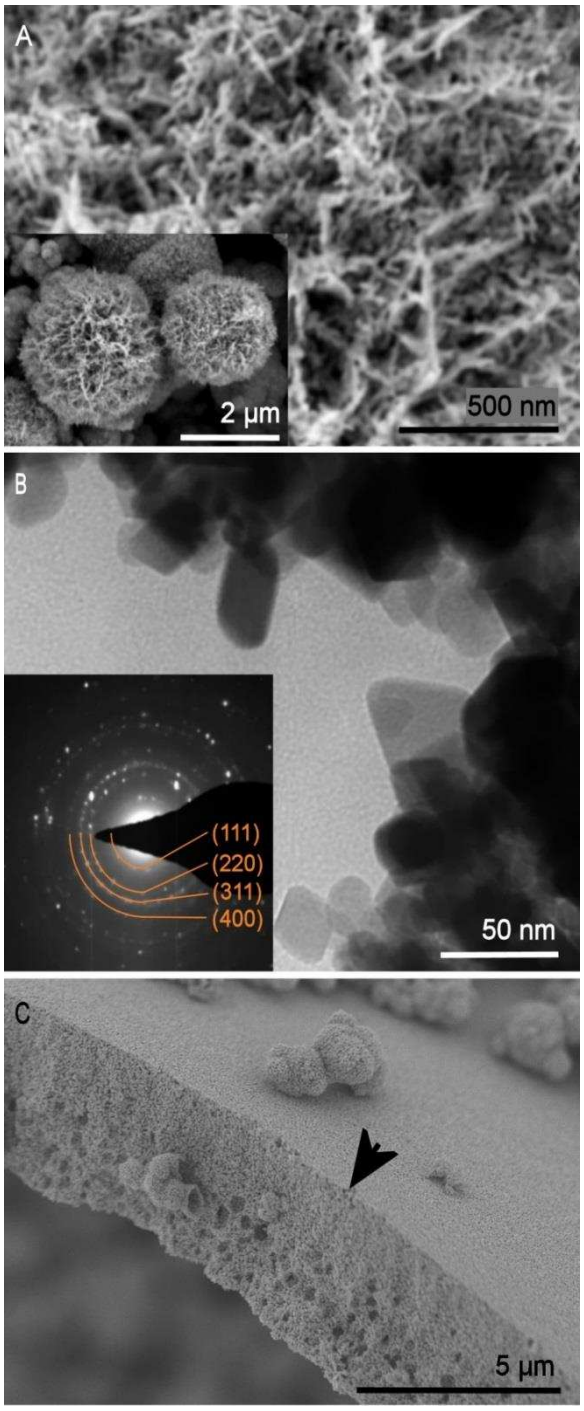

Figure 2. Microstructure of a sample after calcination at 400°C for 2 hours. A) SEM image showing the surface topography and overall morphology (inset) of the spherical aggregates. TEM (B) reveals that calcination causes a transformation of the fibrous protrusions seen in the precursor into interconnected bulkier nanoparticles. The electron diffraction pattern of these aggregates (inset) demonstrates conversion to spinel-type cobalt oxide. C) Interface-grown film fragment with porous structure after calcination. The arrow head points to the air-exposed side of the film.

Transmission electron microscopy (TEM) examination of the microspheres showed that while the films exhibited smooth surfaces, the spheres were covered with fine protrusions 50 – 100 nm in length (Figs. 1E and 1F), as has also been observed for basic cobalt salts produced under hydrothermal conditions.[17] Notably, these spherical particles exhibited high surface areas of 142 $m^2 \cdot g^{-1}$, as evidenced by nitrogen adsorption experiments. The chemical composition of the precipitated material was characterized using a range of techniques and identical compositions were found for both the films and microspheres. Infra-red (IR) spectra (Fig. S2) of precipitates generated after both 6 hours and 48 hours reaction times were consistent with basic cobalt carbonate $Co(CO_3)_x(OH)_y$ (see SI for analysis), while simultaneous thermogravimetric analysis (TGA) and differential scanning calorimetry (DSC) revealed a sharp exothermal peak at 227.5 °C that was accompanied by a mass loss of 19.4 wt % (Fig. S2). This is indicative of the elimination of CO_2 and H_2O during the chemical transformation from $Co(CO_3)_x(OH)_y$ to spinel-Co_3O_4 in air.[61] Calcination of this basic cobalt carbonate precursor at 400 °C resulted in the formation of spinel-type cobalt (II,III) oxide, as confirmed by powder x-ray diffraction (PXRD, Fig. S3), and selected area electron diffraction (SAED, Fig. 2B, inset).[62] SEM showed that the general morphologies of both the microspheres (Fig. 2A) and sheets (Fig. 2C) were retained after annealing, but that the fibrous protrusions on the spheres now comprised distinct 20 – 50 nm nanoparticles which appeared clearly facetted and sometimes elongated in shape (Figs. 2A and 2B). The specific surface areas of the microspheres reduced to 52 $m^2 \cdot g^{-1}$ on annealing.

2. Tobacco Mosaic Viruses as Biotemplates for the Precipitation of Basic Cobalt Carbonate

Tobacco mosaic virus (TMV, schematically illustrated in Figure 3A) was then used to template the formation of more complex morphologies, where the ability of certain divalent cations to induce the ordered aggregation of TMV[63] introduces the intriguing possibility that this effect can be exploited to generate hierarchically structured cobalt (II,III) oxide.

2.1 Aggregate Structures of TMV Formed by Co (II)-Coordination. Addition of a small amount (0.1 $g \cdot L^{-1}$) of TMV to a 100 mM Co (II) solution resulted in the immediate formation of turbidity (Fig. 3 (inset in C)), which is consistent with the generation of aggregates of TMV. While TMV colloids are known to assemble into liquid-crystalline phases in aqueous solution at concentrations above 60 $g \cdot L^{-1}$,[63] metal ions are required to mediate assembly at the low concentrations employed here. That this effect is observed for a number of divalent transition metal cations including Cd^{2+}, Cu^{2+} and Ni^{2+}, but not Ca^{2+} or Mg^{2+} [64] has been ascribed to the presence of specific, low-affinity binding sites on the surface of every CP subunit, which allow for the coordination of the transition metal ions.[63] Interestingly, Ba^{2+} ions have been shown to induce the formation of crystalline superlattices of hexagonally packed TMV in dilute solutions, where this observation was explained by like-charge attraction.[65]

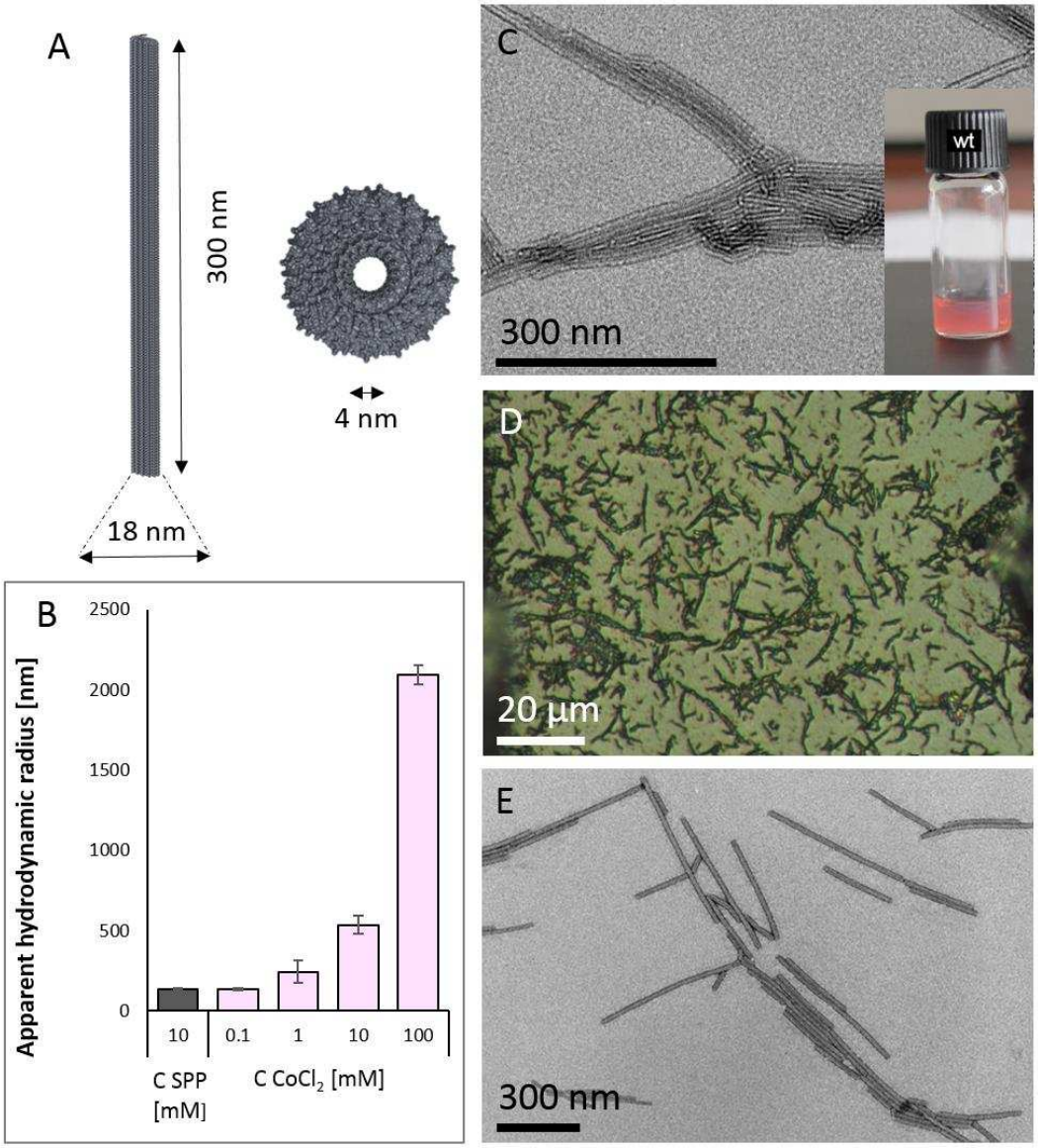

Figure 3. Properties of TMV in $CoCl_2$ solutions. A) Schematic view showing the dimensions of TMV. B) Apparent hydrodynamic radii of TMV/ $CoCl_2$ complexes in solutions containing 0.1 $g \cdot L^{-1}$ TMV and different $CoCl_2$ concentrations. C, E) TEM images of stained TMV. C) The pellet fraction of a solution containing 0.1 $g \cdot L^{-1}$ TMV and 100 mM $CoCl_2$ after 5 min centrifugation at 5,000 g. Inset in C): Turbidity occurring in a solution of cobalt ions upon addition of TMV. D) Light microscopy of Co^{2+}/ TMV association complexes isolated from a 100 mM $CoCl_2$ solution containing 0.1 $g \cdot L^{-1}$ TMV. E) Supernatant of a TMV solution (0.1 mg in 10 mM SPP buffer) after 5 min centrifugation at 20,000 g.

Greater insight into the Co (II)-induced phase separation of TMV was gained using dynamic light scattering (DLS), which provides an estimate of the hydrodynamic radii of the aggregates in aqueous solution. DLS measurements were generally performed after centrifugation of solutions at 5,000 g to remove micron-sized aggregates. While an average size of ≈134 nm (as retrieved from the correlation function which does

not consider the particles' rod-shape) was determined for a control sample containing 0.1 $g \cdot L^{-1}$ wild-type TMV in buffer, the hydrodynamic radii of the suspended TMV particles systematically enlarged in the presence of increasing concentrations of Co^{2+} ions (Fig. 3B). At a low concentration of $[Co^{2+}]$ = 0.1 mM, the hydrodynamic radius of particles in the TMV/ metal ion solution was comparable with the freely dispersed viruses. In contrast, hydrodynamic radii of ≈ 245 and ≈ 535 nm were recorded at cobalt concentrations of $[Co^{2+}]$ = 1 mM and $[Co^{2+}]$ = 10 mM respectively, and a dramatic increase to ≈2,100 nm was observed at $[Co^{2+}]$ = 100 mM.

TEM examination of the re-suspended pellet fraction obtained from a solution containing 100 mM Co^{2+} and 0.1 $g \cdot L^{-1}$ TMV (after centrifugation at 5000g) supported the DLS measurements and revealed the presence of micron-sized fibres and bundles of fibres of TMV (Fig. 3C, enlarged view shown in Fig. S4). Examination of the same solution prior to centrifugation using light microscopy showed high aspect ratio fibres of around 10-20 µm in length (Fig. 3D). In contrast TEM examination of cobalt-free buffer solutions of TMV revealed individual virus particles, together with some oligomeric aggregates (Fig. 3E). The zeta potential of TMV as a function of Co (II) concentration was also measured to determine the relationship between the surface charge and colloidal stability of the virus/ metal aggregates. The data demonstrate that the zeta potential decreases in magnitude with increasing cobalt (II) for $[Co^{2+}] \geq 1$ mM (Fig. S4) and eventually reached a very small negative value of about -2.5 mV in a solution of $[Co^{2+}]$ = 100 mM. For comparison, the bare virus in 10 mM SPP buffer showed a significantly lower zeta potential of -33.6 ± 2.4 at pH = 7.2 and -28.4 ± 2.4 at pH = 4.9. This indicates that the negative surface net charge of the virus particles was almost completely screened by association with the counter-ions. In combination with DLS and TEM, these results point to a substantial aggregation of TMV driven by the association of cobalt ions at $[Co^{2+}]$ = 100 mM, eventually leading to precipitation from the reactant solution.

2.2 Mineralization of Self-Assembled TMV Aggregates.

(i) Characterization of TMV/ Mineral Precipitates. The micron-sized TMV/ Co (II) assemblies formed in solutions of 100 mM Co^{2+} and 0.1 $g \cdot L^{-1}$ TMV were then used as templates to direct the precipitation of basic cobalt carbonate, where this was achieved by transferring the phase-separated TMV/ Co^{2+} mixture to a desiccator followed by exposure to ammonium carbonate vapor for 2 days. This resulted in the formation of a voluminous pale pink precipitate, which was extracted by centrifugation and washed with water and ethanol. SEM examination of the templated material revealed the presence of 20 µm long cylindrical particles (Figs. 4 and S5), together with a small fraction (< 10%) of thin mineral sheets (Fig. S5). A substantial proportion of cylindrical particles were hollow, having inner diameters of 500 nm – 2 µm and wall thicknesses of 100 – 500 nm (Figs. 4A and S5). This was also supported by polarized light microscopy (Fig. S5, inset), where the edges of the elongated particles appeared bright, while the inner channel remained

dark. These structures are therefore comparable in size to the fibres and fibre bundles formed prior to mineralization (Fig. 3D).

While the biogenic templates exerted a dramatic effect on the morphology of the mineral deposits (Figs. 4 and S5), the chemical composition of the mineral phase was largely unaffected by the virus-mediated growth conditions, and IR spectroscopy and thermal analysis both showed structural features very similar to those of purely inorganic basic cobalt carbonate (Figs. 4C and S6). That the TMV coat proteins (CPs) are both intimately associated with the mineral phase and also remain intact during mineralization was conclusively demonstrated by dissolving the precipitates and then performing SDS-gel electrophoresis followed by western blotting and immunostaining of the TMV coat protein (CP) with specific antibodies. Non-degraded virus CP was demonstrated for aggregates generated at $[Co^{2+}]$ = 100 mM and [TMV] = 0.1 $g \cdot L^{-1}$ (Figure S7, line 1), and at higher occlusion levels on increasing [TMV] to 0.5 $g \cdot L^{-1}$ (Figure S7, line 2).

The importance of the slow mineralization conditions in generating the hierarchical cobalt carbonate structures was demonstrated by conducting a rapid mineralization in which a $CoCl_2$ solution containing TMV was mixed with a 100 mM solution of ammonium carbonate, and the resulting precipitate was then aged for 2 days. This led to large masses of poorly crystalline, gel-like product (Fig. S8). The concentration of TMV present also governed the formation of the TMV/ mineral products, as demonstrated by performing the reaction at a reduced virus particle concentration of 0.02 $g \cdot L^{-1}$, while maintaining $[Co^{2+}]$ = 100 mM. Under these conditions, the precipitate still comprised mineral sheets and rods with similar sizes to those formed at [TMV] = 0.1 $g \cdot L^{-1}$ (Fig. S9), but only ≈ 75% of the precipitates were rods as compared with ≈ 90% at [TMV] = 0.1 $g \cdot L^{-1}$.

(ii) *Analysis of Calcination Products.* The TMV/ mineral assemblies were then converted to spinel-type Co_3O_4 by calcining at 400°C, as confirmed by XRD (Fig. S10) and Raman spectroscopy (Fig. 5A).[66, 67] Although the virus particles can be expected to decompose under these annealing conditions (Fig. S6), the gross morphologies of the tubes remained intact after calcination (Fig. 4D). Significant changes were, however, observed on the submicrometer length scale, were the hairy protrusions of the precursor particles where replaced with individual nanograins (Fig. 5B vs. Figs. 4D and 5C). These interconnected particles measured ≈ 20 nm in size and exhibited smooth facets (Fig. 5C). Some of the nanoparticles also showed elongated shapes, which is atypical for cubic Co_3O_4 (inset in Fig. 5C). TEM of these annealed tubes revealed the presence of nanoscale pores between the Co_3O_4 grains (Fig. 5C), where these likely arise due to shrinkage of the material during elimination of water and carbon dioxide.

Measurement of the surface areas of the TMV/ mineral nanorods showed that the BET surface area decreased from 98 $m^2 \cdot g^{-1}$ to 20 $m^2 \cdot g^{-1}$ during the annealing procedure. This indicates that the coarsening of the fine fibres on the surfaces of the particles on calcination overcompensates for the gain in surface

area due to pore formation. It is notable, however, that the final surface areas of 52 $m^2 \cdot g^{-1}$ and 20 $m^2 \cdot g^{-1}$ achieved under additive-free and virus-mediated growth are comparable to typical values for porous Co_3O_4 microparticles prepared by calcination of cobalt carbonates synthesized under hydrothermal conditions.[18] In comparison, powders of Co_3O_4 nanoparticles with average sizes of 21 nm,[68] 11 nm,[69] and 6 nm[68] have been reported to exhibit surface areas of 28 $m^2 \cdot g^{-1}$, 77 $m^2 \cdot g^{-1}$, and 111 $m^2 \cdot g^{-1}$, respectively.

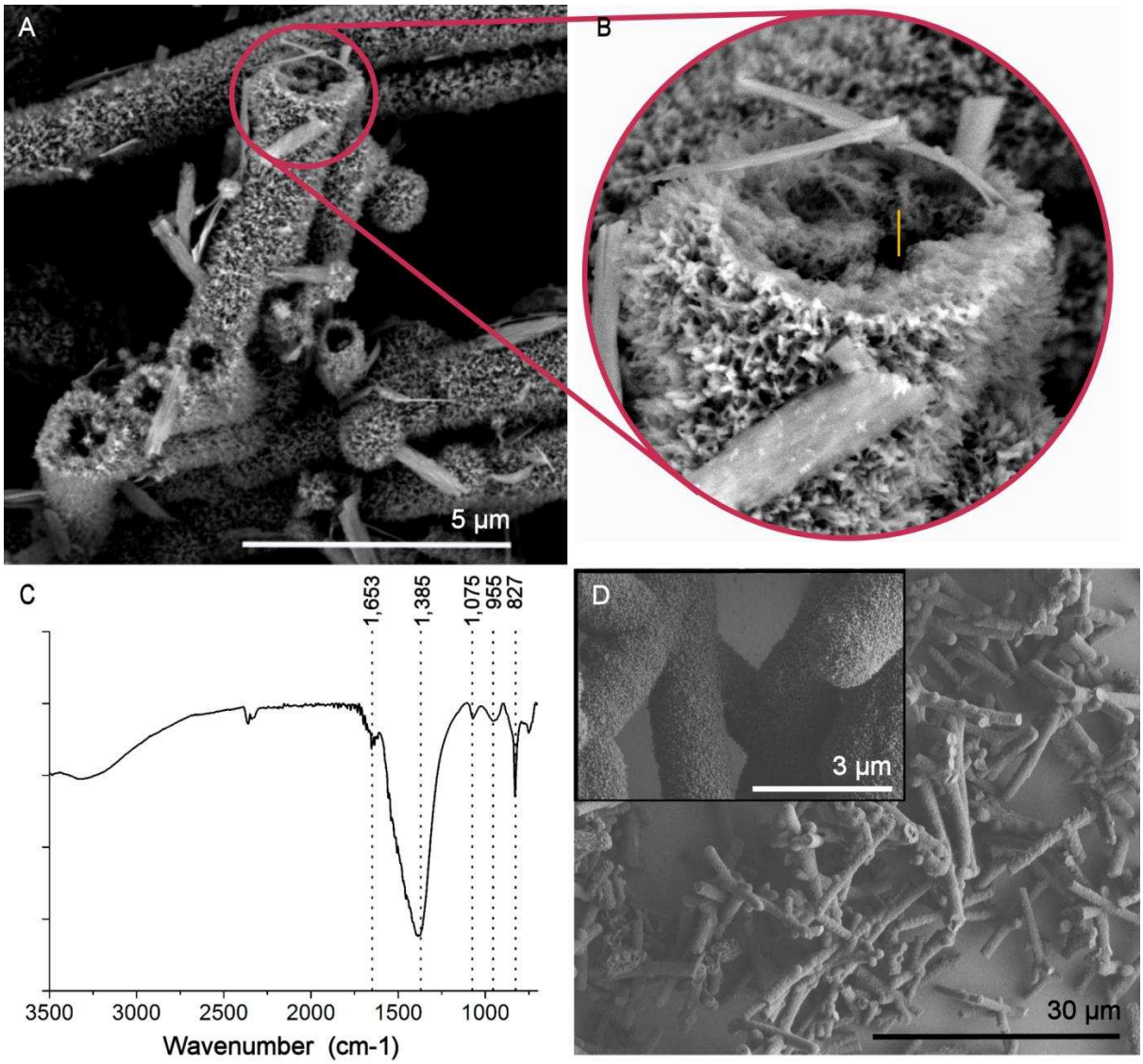

Figure 4. TMV/ mineral composites prepared via ammonium carbonate diffusion. A, B) SEM images showing mineralized rods or tubes precipitated from a solution containing [Co2+] = 100 mM and [TMV] = 0.1 g·L-1. A) The cylindrical particles show rough surfaces, and some of them appear hollow. B) Cross section of a representative tube, where the yellow bar indicates the dimensions of an individual virus. C) IR spectrum of a precipitate obtained from a solution containing [Co2+] = 100 mM and [TMV] = 0.1 g·L-1 after 48 hours reaction time. D) SEM images of Co_3O_4 mineral rods and tubes formed by annealing the TMV/ mineral precursor (400°C, 2 hours), showing the preservation of the overall morphology. Inset: Higher magnification image of the surface structure.

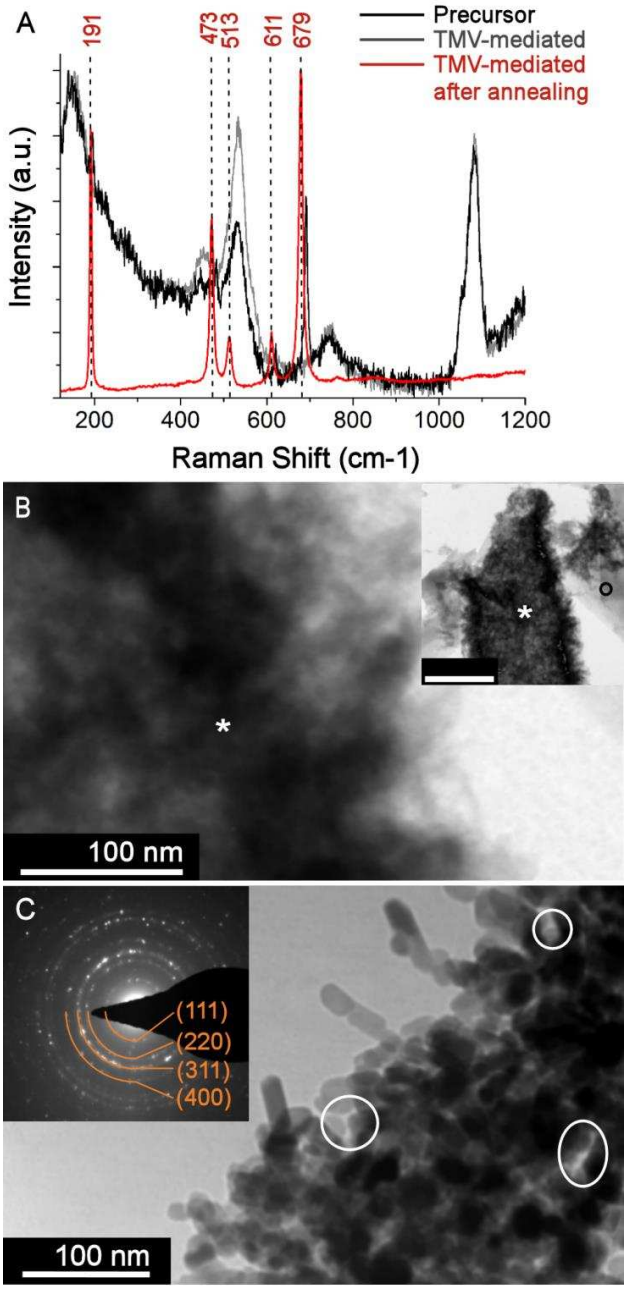

Figure 5. Transformation of TMV/ basic cobalt carbonate into a superstructure of Co_3O_4. A) Raman spectra of basic cobalt carbonate formed in the absence (black line) or presence (grey line) of TMV. Vibration bands characteristic of Co_3O_4 are seen after calcination of the TMV/ precursor rods and tubes at 400°C. B) TEM image of a microtube (*) composed of basic cobalt carbonate and TMV. Inset in B: Lower magnification image of the same particle. The rods and tubules (*) are accompanied by a minor fraction of thin sheet-like mineral structures (o). Scale bar (Inset) = 500 nm. C) Distinct nanoparticle units are seen on the surface of the rods and tubes after calcination. The encircled areas highlight voids between the nanoparticle units. The electron diffraction pattern (inset) is consistent with the Co_3O_4 lattice structure.

3. Electrocatalytic Activity Towards the Oxygen Evolution Reaction (OER)

A number of previous reports have shown that the catalytic activity of cobalt (II,III) oxide in electrochemical water splitting, or more specifically in the oxygen evolution reaction (OER), critically depends on the size and shape of the inorganic particles.[7, 70-72] Our methodology – which affords the ability to generate hierarchically-ordered Co_3O_4 structures – therefore provides a unique opportunity to investigate the role of morphological control in the design of these catalysts. We therefore measured the overpotentials with respect to the OER for the nanoparticle-based superstructures generated in the absence and presence of TMV and compared these to a commercially available cobalt (II,III) oxide nanopowder comprising aggregated particles with irregular shapes.

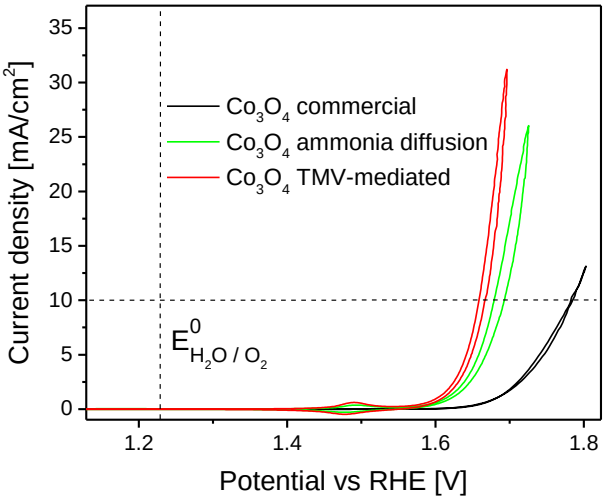

Figure 6. OER performance of cobalt oxide materials with different morphologies. Cyclic voltammograms (I/E-curves) are presented for a commercial Co_3O_4 nanopowder (black curve), Co_3O_4 prepared by ammonia diffusion in the absence of additives (green curve) and TMV-directed Co_3O_4 (red curve). Data were recorded in 0.1 M NaOH electrolyte at a scan rate of 10 mV/s at 2,000 r.p.m.. The vertical dashed line indicates the position of E^o (H_2O/O_2) and the horizontal dashed line marks the current density of 10 mA/cm^2, at which the overpotentials $\eta_{i=10mA/cm^2}$ were determined.

For these experiments the different metal oxide powders were immobilized on glassy carbon (GC) electrodes with oxide loadings of either 0.25 mg/cm^2 or 1.4 mg/cm^2 (Fig. S11). SEM confirmed a homogeneous distribution of the catalyst particles on the electrode surface (Fig. S12). Cyclic voltammetry was performed in alkaline solution (0.1 M NaOH) to determine the overpotential $\eta_{i=10mA/cm^2}$ for the OER, which is defined as the difference between the theoretical standard potential of the reaction $4\ OH^- \rightarrow 2\ H_2O + O_2 + 4\ e^-$ (1.229 V vs the reversible hydrogen

electrode (RHE)) and the measured potential required to reach a current density of 10 mA/cm^2.[73] Figure 6 shows representative I/E-curves obtained with the differently shaped Co_3O_4 materials at an oxide loading of 0.25 mg/cm^2 on the electrode. I/E-curves of electrodes fabricated with an oxide loading of 1.4 mg/cm^2 confirmed that the measured overpotentials did not depend on the electrode preparation (Fig. S13).

The cyclic voltammograms obtained from all three Co_3O_4 samples showed a redox couple at 1.48 V vs RHE related to the Co (III)/ Co (IV) transition of spinel-type cobalt oxide[74, 75] prior to the onset of the OER. Remarkably, while we observed a moderate value of $\eta_{i=10mA/cm^2}$ = 548 ± 10 mV for the overpotential of the commercial Co_3O_4 nanopowder (black curve), significantly lower overpotentials were measured for the materials prepared by calcination of ammonia diffusion-grown basic carbonate precursors, both in the absence (green curve) and presence of TMV (red curve). Specifically, a decrease of 87 mV was determined for the urchin-like Co_3O_4 microparticles (including a minor fraction of mineral sheets) generated in the absence of TMV ($\eta_{i=10mA/cm^2}$ = 461 ± 11 mV). Most strikingly, the highly anisotropic rod-shaped and tubular superstructures obtained by virus-directed mineralization exerted an even more dramatic effect, reducing the overpotential by 112 mV ($\eta_{i=10mA/cm^2}$ = 436 ± 13 mV). These data clearly show that the hierarchically structured, virus-directed cobalt oxide particles exhibit a superior catalytic activity towards the OER to conventionally prepared Co_3O_4. SEM micrographs of TMV-directed Co_3O_4 particles recorded before and after performance as an OER catalyst at 10 mA/cm^2 for 10 minutes confirmed that the structure of the microrods and -tubes was preserved during the reaction (Fig. S14).

Discussion

Providing an intriguing example for the bio-templated synthesis of Co_3O_4 at room temperature, Belcher and co-workers have decorated M13-bacteriophages with cobalt (II,III)-oxide nanoparticles, where the resulting virus/ oxide nanowires have shown excellent performance as an anode material in lithium ion batteries.[36] In contrast to these very thin and flexible M13 nanotemplates, the TMV particles applied in our study exhibit a more rigid supramolecular structure. TMV-like nanorod derivatives can be formed *in vitro* by bottom-up assembly of CP units with RNA,[45] which enables tailored modifications of both their size and shape,[46] and the introduction of selected functional groups.[47] This renders these nanotubular protein/ RNA complexes a highly versatile scaffold material.[76-78]

In view of synthetic strategies to generate mesostructured functional materials, the nanoscale dimensions and inherently very narrow size distributions of TMV and TMV-like particles have

made the prospect of mineralizing pre-assembled ordered aggregates of these rod-shaped nanoparticles highly attractive. Indeed, the formation of well-ordered liquid crystalline phases of TMV is well-documented at high virus concentrations[63, 79] and such phases have been successfully applied as templates for mineral deposition.[80] As an early demonstration of this concept, Fowler *et al.* have prepared mesostructured silica by infiltrating a gel-like nematic phase formed by self-organization of highly concentrated TMV particles ([TMV] = 16 $g \cdot L^{-1}$).[80]

Contrastingly, our study on the virus-mediated deposition of basic cobalt carbonate makes use of the metal-ion induced pre-organization of biotemplates directly in the Co (II)-containing reactant solution, which is very dilute with respect to the TMV concentration ([TMV] = 0.1 $g \cdot L^{-1}$). In such a dilute regime, the protein/ RNA nanorods would be expected to form stable colloidal solutions in the absence of metal ions. The observation of a spontaneous phase separation, therefore, suggests that Co (II) binds to the virus particles, which then promotes the formation of micron-sized association complexes composed of TMV cross-linked by the cations. In fact, based on their chemical composition comprising mainly hydrophilic amino acids, TMV particles represent polyelectrolytes with an isoelectric point at pH = 3.5.[81] The reactant solution we have used for mineralization ([Co^{2+}] = 100 mM and [TMV] = 0.1 $g \cdot L^{-1}$) exhibits a starting pH of 4.5, which then further increases to 10 during the course of the reaction. Therefore, the virus nanorods can be expected to carry a negative net charge, which facilitates favorable electrostatic interactions with Co (II) cations, under the pH conditions at which basic cobalt carbonate is precipitated. In similarity with previous reports on the ordered association of TMV in the presence of Cd (II) ions, Co (II) coordination may be achieved via specific, low-affinity binding sites exposed on the surface of every CP subunit, which exist in addition to two well-characterized internal metal binding sites.[63]

Remarkably, in our study the preparation of Co_3O_4 by depositing a thermally unstable basic cobalt carbonate precursor via co-precipitation with tobacco mosaic viruses, has led to the formation of an unusual hierarchically structured product, composed of spinel oxide nanoparticles arranged in rod-like or tubular superstructures in the size range of tens of micrometers. Compared with isolated nanoparticles, such mesostructured materials bear the advantage of improved stability and processability and potentially even enable cooperative effects between the nanoparticle units, where this can affect the resulting functional properties.[2, 82-84]

When analyzing the Co_3O_4 materials prepared in our study in view of potential applications as an electrocatalyst for the OER, the virus-directed Co_3O_4 microrods and tubes have shown particularly desirable properties. Representing a critical half-cell reaction in electrochemical water splitting, the OER involves a complex four-electron transfer leading to poor reaction kinetics.[85] This generates an enormous demand for robust and efficient catalysts to promote this redox process and the overpotential required for the OER is widely recognized as a figure of merit for the electrocatalytic activity of a material. This property describes a kinetic barrier determined by mass-transport limitations[86] as well as the binding affinity of reaction intermediates to the catalyst surface[87]. Therefore, the overpotential depends on structural parameters such as the availability and accessibility of active sites for chemisorption on the catalyst surface,[6, 73] which highlights the importance of the crystallographic facets exposed by the catalyst particles as well as the defect structure of the crystalline domains.[86] Another critical parameter determining the electrocatalytic activity of a material is the electrical conductivity, which is associated with efficient electron transfer.[88] Building on these considerations, synthetic strategies based on compounding catalyst nanoparticles with conducting carbon species have also been explored.[89, 90] Notably, a reduction of the onset potential for the OER by 50 mV was achieved by An *et al.* when Co_3O_4 nanoparticles were loaded with an optimum density of N-doped Vulcan carbon.[89]

In our experiments the overpotential was lowered by 112 mV in the virus-directed material as compared to a commercial nanopowder of Co_3O_4 (Sigma Aldrich, <50 nm particle size). This convincingly demonstrates the critical role of catalyst nanostructure. Morphologically, the virus-directed material, therefore, appears to offer a particularly favorable combination of a nanogranular substructure, which leads to a high surface area, and a tubular microstructure that facilitates the transport of the reactants and gaseous products. Notably, Xu *et al.* have recently reported on an improved electrocatalytic performance of hydrothermally synthesized urchin-like Co_3O_4-spheres as compared to layered Co_3O_4, where this effect was in parts attributed to the facilitation of bubble release at the rough-textured catalyst surface.[91]
We speculate that nanostructuring the basic carbonate precursor by TMV-templating may additionally affect the morphology of the individual Co_3O_4 nanograins formed after calcination, such that crystallographic facets with a high density of catalytic centers are exposed on the particle surface, thus lowering the activation energy for the redox event. In a broader context, hollow structures of cobalt (II,III) oxide are currently extensively investigated for a variety of

applications including supercapacitors, lithium ion batteries, and magnetic structures due to their light-weight architecture and their diverse range of intriguing functional properties.[92]

Conclusions and Outlook

In conclusion, these experiments demonstrate that generation of basic cobalt carbonate via ammonium carbonate diffusion at room temperature provides a slow, aqueous phase synthesis of this material. This then opens the door to structural control using bio-inspired routes. Exploiting tobacco mosaic virus (TMV) as a versatile template, we demonstrate that added Co (II) ions drive the oriented assembly of the virus nanoparticles, leading to the formation of micron-scale fibres and bundles of fibres. Mineralization of these structures then generates basic cobalt carbonate with unusual rod-like and tubular composite structures, which can be readily converted to spinel-type Co_3O_4 on annealing at 400°C. Notably, this is achieved with a retention of the gross morphology and the resultant oxide rods and tubes exhibit hierarchical structures which comprise interconnected nanoparticles. We then show that these Co_3O_4 superstructures exhibit superior catalytic performance in the oxygen evolution reaction as compared to a commercial nanopowder. The strategy of mineralizing pre-assembled virus particles opens up interesting prospects for the design of bio-inorganic composites. Beyond the use of plant-derived wild type TMV, modern methods in molecular biology and chemistry allow the controlled variation of size, shape and surface-exposed functional groups of TMV derivatives. This in turn enables the preparation of virus-like templates exhibiting different net charges, metal binding capacities and supramolecular structures, where these could be tailored towards particular ultrastructures and mineral products.[46, 47, 53, 93-95]

Acknowledgements

S.L and A.S.S. acknowledge funding by the Carl Zeiss Foundation in the framework of a postdoctoral fellowship and by the DFG via the Emmy Noether programme (LU 1445/2-1). The Fonds der Chemischen Industrie is thanked for a material cost allowance. We are grateful for additional support received from the DFG via priority program SPP1569 “Generation of Multifunctional Inorganic Materials by Molecular Bionics” (grants DFG-WE-4220/2-2 and /3-1, EI 901/1-2 and /2-1). The Carl-Zeiss Foundation is gratefully acknowledged for funding the interdisciplinary Projekthaus NanoBioMater with the University of Stuttgart. We thank the Engineering and Physical Sciences Research Council (EPSRC) for financial support via grants EP/G00868X/1 (A.K. and F.C.M.) and EP/N002423/1 (F.C.M.). Furthermore, the authors are

thankful to Christoph Schneck and Christian Funk for thermal analysis, to Manuel Roussel and Michael Schweikert for assistance in TEM measurements, and to Marc Widenmeyer for PXRD measurements. Diether Gotthardt is thanked for taking care of the plants, and Sigrid Kober and Rebecca Hummel for technical assistance.

Notes and references

1. D. Su, X. Xie, P. Munroe, S. Dou and G. Wang, *Scientific Reports*, 2014, **4**, 6519.
2. Y. Liu, G. Zhu, B. Ge, H. Zhou, A. Yuan and X. Shen, *CrystEngComm*, 2012, **14**, 6264-6270.
3. X. Xie, Y. Li, Z.-Q. Liu, M. Haruta and W. Shen, *Nature*, 2009, **458**, 746-749.
4. P. W. Menezes, A. Indra, N. R. Sahraie, A. Bergmann, P. Strasser and M. Driess, *ChemSusChem*, 2015, **8**, 164-171.
5. R. J. Toh, A. Y. S. Eng, Z. Sofer, D. Sedmidubsky and M. Pumera, *ChemElectroChem*, 2015, **2**, 982-987.
6. H. Zhao, Y.-P. Zhu and Z.-Y. Yuan, *European Journal of Inorganic Chemistry*, 2016, **2016**, 1916-1923.
7. J. A. Koza, Z. He, A. S. Miller and J. A. Switzer, *Chemistry of Materials*, 2012, **24**, 3567-3573.
8. V. R. Shinde, S. B. Mahadik, T. P. Gujar and C. D. Lokhande, *Applied Surface Science*, 2006, **252**, 7487-7492.
9. A. U. Mane, K. Shalini, A. Wohlfart, A. Devi and S. A. Shivashankar, *Journal of Crystal Growth*, 2002, **240**, 157-163.
10. B. Han, J.-M. Park, K. H. Choi, W.-K. Lim, T. R. Mayangsari, W. Koh and W.-J. Lee, *Thin Solid Films*, 2015, **589**, 718-722.
11. K. Ding, X. Zhang, P. Yang and X. Cheng, *CrystEngComm*, 2016.
12. D. Wang, Q. Wang and T. Wang, *Inorganic Chemistry*, 2011, **50**, 6482-6492.
13. Z. Wang, X. Chen, M. Zhang and Y. Qian, *Solid State Sciences*, 2005, **7**, 13-15.
14. J. Zhao, X. Zhang, M. Li, S. Lu and P. Yang, *CrystEngComm*, 2016, **18**, 8020-8029.
15. T. Ghosh, S. K. Dash, P. Chakraborty, A. Guha, K. Kawaguchi, S. Roy, T. Chattopadhyay and D. Das, *RSC Advances*, 2014, **4**, 15022-15029.
16. J. Yang, H. Cheng and R. L. Frost, *Spectrochimica Acta Part A: Molecular and Biomolecular Spectroscopy*, 2011, **78**, 420-428.
17. Y. Zhang, B. Cui, O. Derr, Z. Yao, Z. Qin, X. Deng, J. Li and H. Lin, *Nanoscale*, 2014, **6**, 3376-3383.
18. H.-P. Cong and S.-H. Yu, *Crystal Growth & Design*, 2009, **9**, 210-217.

19. M. A. Garakani, S. Abouali, B. Zhang, Z.-L. Xu, J. Huang, J.-Q. Huang, E. K. Heidari and J.-K. Kim, *Journal of Materials Chemistry A*, 2015, **3**, 17827-17836.
20. R. Yu, P. Tao, X. Zhou and Y. Fang, *Journal of Alloys and Compounds*, 2008, **461**, 574-578.
21. E. Beniash, *Wiley Interdisciplinary Reviews: Nanomedicine and Nanobiotechnology*, 2011, **3**, 47-69.
22. A. S. Schenk and Y.-Y. Kim, *MRS Bulletin*, 2015, **40**, 499-508.
23. P. Fratzl and R. Weinkamer, *Progress in Materials Science*, 2007, **52**, 1263-1334.
24. Y.-Y. Kim, J. D. Carloni, B. Demarchi, D. Sparks, D. G. Reid, M. E. Kunitake, C. C. Tang, M. J. Duer, C. L. Freeman, B. Pokroy, K. Penkman, J. H. Harding, L. A. Estroff, S. P. Baker and F. C. Meldrum, *Nature Materials*, 2016, **15**, 903-910.
25. B. Cantaert, Y.-Y. Kim, H. Ludwig, F. Nudelman, N. A. J. M. Sommerdijk and F. C. Meldrum, *Advanced Functional Materials*, 2012, **22**, 907-915.
26. L. B. Gower and D. J. Odom, *Journal of Crystal Growth*, 2000, **210**, 719-734.
27. A. S. Schenk, B. Cantaert, Y.-Y. Kim, Y. Li, E. S. Read, M. Semsarilar, S. P. Armes and F. C. Meldrum, *Chemistry of Materials*, 2014, **26**, 2703-2711.
28. T. Wang, H. Cölfen and M. Antonietti, *Journal of the American Chemical Society*, 2005, **127**, 3246-3247.
29. A. S. Schenk, I. Zlotnikov, B. Pokroy, N. Gierlinger, A. Masic, P. Zaslansky, A. N. Fitch, O. Paris, T. H. Metzger, H. Cölfen, P. Fratzl and B. Aichmayer, *Advanced Functional Materials*, 2012, **22**, 4668-4676.
30. A. N. Kulak, P. Iddon, Y. Li, S. P. Armes, H. Cölfen, O. Paris, R. M. Wilson and F. C. Meldrum, *Journal of the American Chemical Society*, 2007, **129**, 3729-3736.
31. R.-Q. Song, A.-W. Xu, M. Antonietti and H. Cölfen, *Angewandte Chemie International Edition*, 2009, **48**, 395-399.
32. Y.-J. Han and J. Aizenberg, *Angewandte Chemie International Edition*, 2003, **42**, 3668-3670.
33. B. R. Heywood and S. Mann, *Langmuir*, 1992, **8**, 1492-1498.
34. A. S. Finnemore, M. R. J. Scherer, R. Langford, S. Mahajan, S. Ludwigs, F. C. Meldrum and U. Steiner, *Advanced Materials*, 2009, **21**, 3928-3932.
35. S. Ludwigs, U. Steiner, A. N. Kulak, R. Lam and F. C. Meldrum, *Advanced Materials*, 2006, **18**, 2270-2273.
36. K. T. Nam, D.-W. Kim, P. J. Yoo, C.-Y. Chiang, N. Meethong, P. T. Hammond, Y.-M. Chiang and A. M. Belcher, *Science*, 2006, 10.1126/science.1122716.

37. W. Shenton, T. Douglas, M. Young, G. Stubbs and S. Mann, *Advanced Materials*, 1999, **11**, 253-256.
38. B. Aichmayer, M. Mertig, A. Kirchner, O. Paris and P. Fratzl, *Advanced Materials*, 2006, **18**, 915-919.
39. S. R. Hall, H. Bolger and S. Mann, *Chemical Communications*, 2003, 2784-2785.
40. B. Wucher, W. Yue, A. N. Kulak and F. C. Meldrum, *Chemistry of Materials*, 2007, **19**, 1111-1119.
41. W. Yue, R. J. Park, A. N. Kulak and F. C. Meldrum, *Journal of Crystal Growth*, 2006, **294**, 69-77.
42. N. C. Bigall, M. Reitzig, W. Naumann, P. Simon, K.-H. van Pée and A. Eychmüller, *Angewandte Chemie International Edition*, 2008, **47**, 7876-7879.
43. M. Knez, A. M. Bittner, F. Boes, C. Wege, H. Jeske, E. Maiβ and K. Kern, *Nano Letters*, 2003, **3**, 1079-1082.
44. J. M. Alonso, M. Ł. Górzny and A. M. Bittner, *Trends in Biotechnology*, 2013, **31**, 530-538.
45. A. Mueller, F. J. Eber, C. Azucena, A. Petershans, A. M. Bittner, H. Gliemann, H. Jeske and C. Wege, *ACS Nano*, 2011, **5**, 4512-4520.
46. F. J. Eber, S. Eiben, H. Jeske and C. Wege, *Nanoscale*, 2015, **7**, 344-355.
47. F. C. Geiger, F. J. Eber, S. Eiben, A. Mueller, H. Jeske, J. P. Spatz and C. Wege, *Nanoscale*, 2013, **5**, 3808-3816.
48. A. M. Bittner, F. Heber and J. Hamaekers, *Surface Science*, 2009, **603**, 1922-1925.
49. K. Wadu-Mesthrige, B. Pati, W. M. McClain and G.-Y. Liu, *Langmuir*, 1996, **12**, 3511-3515.
50. Z. Wu, A. Mueller, S. Degenhard, S. E. Ruff, F. Geiger, A. M. Bittner, C. Wege and C. E. Krill Iii, *ACS Nano*, 2010, **4**, 4531-4538.
51. E. Dujardin, C. Peet, G. Stubbs, J. N. Culver and S. Mann, *Nano Letters*, 2003, **3**, 413-417.
52. E. Royston, A. Ghosh, P. Kofinas, M. T. Harris and J. N. Culver, *Langmuir*, 2008, **24**, 906-912.
53. K. Gerasopoulos, M. McCarthy, E. Royston, J. N. Culver and R. Ghodssi, *Journal of Micromechanics and Microengineering*, 2008, **18**, 104003.
54. P. Atanasova, D. Rothenstein, J. J. Schneider, R. C. Hoffmann, S. Dilfer, S. Eiben, C. Wege, H. Jeske and J. Bill, *Advanced Materials*, 2011, **23**, 4918-4922.
55. N. Stitz, S. Eiben, P. Atanasova, N. Domingo, A. Leineweber, Z. Burghard and J. Bill, *Scientific Reports*, 2016, **6**.

56. K. Altintoprak, A. Seidenstücker, A. Welle, S. Eiben, P. Atanasova, N. Stitz, A. Plettl, J. Bill, H. Gliemann, H. Jeske, D. Rothenstein, F. Geiger and C. Wege, *Beilstein Journal of Nanotechnology*, 2015, **6**, 1399-1412.
57. S. Fujikawa and T. Kunitake, *Langmuir*, 2003, **19**, 6545-6552.
58. M. Gnerlich, H. Ben-Yoav, J. N. Culver, D. R. Ketchum and R. Ghodssi, *Journal of Power Sources*, 2015, **293**, 649-656.
59. V. P. Tolstoy and L. B. Gulina, *Langmuir*, 2014, **30**, 8366-8372.
60. L. B. Gulina and V. P. Tolstoy, *Russian Journal of General Chemistry*, 2014, **84**, 1472-1475.
61. L. Avramov and C. Betschev, *Zeitschrift für anorganische und allgemeine Chemie*, 1971, **383**, 96-102.
62. X. Liu and C. T. Prewitt, *Physics and Chemistry of Minerals*, 1990, **17**, 168-172.
63. A. Nedoluzhko and T. Douglas, *Journal of Inorganic Biochemistry*, 2001, **84**, 233-240.
64. K. Namba, R. Pattanayek and G. Stubbs, *Journal of Molecular Biology*, 1989, **208**, 307-325.
65. T. Li, R. E. Winans and B. Lee, *Langmuir*, 2011, **27**, 10929-10937.
66. V. G. Hadjiev, M. N. Iliev and I. V. Vergilov, *Journal of Physics C: Solid State Physics*, 1988, **21**, L199.
67. M. Rashad, M. Rüsing, G. Berth, K. Lischka and A. Pawlis, *Journal of Nanomaterials*, 2013, **2013**, 6.
68. A. J. Esswein, M. J. McMurdo, P. N. Ross, A. T. Bell and T. D. Tilley, *The Journal of Physical Chemistry C*, 2009, **113**, 15068-15072.
69. S. Farhadi, J. Safabakhsh and P. Zaringhadam, *Journal of Nanostructure in Chemistry*, 2013, **3**, 1-9.
70. H. Jin, J. Wang, D. Su, Z. Wei, Z. Pang and Y. Wang, *Journal of the American Chemical Society*, 2015, **137**, 2688-2694.
71. P. W. Menezes, A. Indra, D. González-Flores, N. R. Sahraie, I. Zaharieva, M. Schwarze, P. Strasser, H. Dau and M. Driess, *ACS Catalysis*, 2015, **5**, 2017-2027.
72. J. Wu, Y. Xue, X. Yan, W. Yan, Q. Cheng and Y. Xie, *Nano Research*, 2012, **5**, 521-530.
73. C. C. L. McCrory, S. Jung, J. C. Peters and T. F. Jaramillo, *Journal of the American Chemical Society*, 2013, **135**, 16977-16987.
74. E. B. Castro, C. A. Gervasi and J. R. Vilche, *Journal of Applied Electrochemistry*, 1998, **28**, 835-841.
75. P. Nkeng, G. Poillerat, J. F. Koenig, P. Chartier, B. Lefez, J. Lopitaux and M. Lenglet, *Journal of The Electrochemical Society*, 1995, **142**, 1777-1783.

76. A. M. Bittner, J. M. Alonso, M. L. Gorzny and C. Wege, *Sub-cellular biochemistry*, 2013, **68**, 667-702.
77. J. N. Culver, A. D. Brown, F. Zang, M. Gnerlich, K. Gerasopoulos and R. Ghodssi, *Virology*, 2015, **479–480**, 200-212.
78. C. Koch, F. J. Eber, C. Azucena, A. Förste, S. Walheim, T. Schimmel, A. M. Bittner, H. Jeske, H. Gliemann, S. Eiben, F. C. Geiger and C. Wege, *Beilstein Journal of Nanotechnology*, 2016, **7**, 613-629.
79. J. Gregory and K. C. Holmes, *Journal of Molecular Biology*, 1965, **13**, 796.
80. C. E. Fowler, W. Shenton, G. Stubbs and S. Mann, *Advanced Materials*, 2001, **13**, 1266-1269.
81. M. Zaitlin, *AAB Description of Plant Viruses, 370, 8 (http://dpvweb.net/dpv/showdpv.php?dpvno=370)*, 2016.
82. X. L. Wu, S. J. Xiong, LiuZ, ChenJ, J. C. Shen, T. H. Li, P. H. Wu and P. K. Chu, *Nature Nanotechnology*, 2011, **6**, 103-106.
83. M.-G. Ma and H. Cölfen, *Current Opinion in Colloid & Interface Science*, 2014, **19**, 56-65.
84. T. Tachikawa and T. Majima, *NPG Asia Materials*, 2014, **6**, e100.
85. W. T. Hong, M. Risch, K. A. Stoerzinger, A. Grimaud, J. Suntivich and Y. Shao-Horn, *Energy & Environmental Science*, 2015, **8**, 1404-1427.
86. H. Dau, C. Limberg, T. Reier, M. Risch, S. Roggan and P. Strasser, *ChemCatChem*, 2010, **2**, 724-761.
87. I. C. Man, H.-Y. Su, F. Calle-Vallejo, H. A. Hansen, J. I. Martínez, N. G. Inoglu, J. Kitchin, T. F. Jaramillo, J. K. Nørskov and J. Rossmeisl, *ChemCatChem*, 2011, **3**, 1159-1165.
88. T. Maiyalagan, K. A. Jarvis, S. Therese, P. J. Ferreira and A. Manthiram, *Nature Communications*, 2014, **5**, 3949.
89. T. An, X. Ge, T. S. A. Hor, F. W. T. Goh, D. Geng, G. Du, Y. Zhan, Z. Liu and Y. Zong, *RSC Advances*, 2015, **5**, 75773-75780.
90. Y. Zhan, G. Du, S. Yang, C. Xu, M. Lu, Z. Liu and J. Y. Lee, *ACS Applied Materials & Interfaces*, 2015, **7**, 12930-12936.
91. Q.-Z. Xu, Q.-Z. Xu, Y.-Z. Su, H. Wu, H. Cheng, Y.-P. Hui, N. Li and Z.-Q. Liu, *Current Nanoscience*, 2014, **11**, 107-112.
92. X. Wang, W. Tian, T. Zhai, C. Zhi, Y. Bando and D. Golberg, *Journal of Materials Chemistry*, 2012, **22**, 23310-23326.
93. P. Atanasova, N. Stitz, S. Sanctis, J. H. M. Maurer, R. C. Hoffmann, S. Eiben, H. Jeske, J. J. Schneider and J. Bill, *Langmuir*, 2015, **31**, 3897-3903.

94. S. Eiben, N. Stitz, F. Eber, J. Wagner, P. Atanasova, J. Bill, C. Wege and H. Jeske, *Virus Research*, 2014, **180**, 92-96.

95. A. Kadri, E. Maiß, N. Amsharov, A. M. Bittner, S. Balci, K. Kern, H. Jeske and C. Wege, *Virus Research*, 2011, **157**, 35-46.